



Role of Alloy Chemistry on Stability of Passive Films in Austenitic Stainless Steel

N. Srinivasan and S. Senthil Kumaran

(Submitted August 28, 2018; in revised form March 25, 2019; published online May 23, 2019)

This study dealt with characterizing oxide passive films in austenitic stainless steels with different chemical compositions. Stacking fault energy was estimated, and thermal conductivity at different temperatures (298, 673, 873 and 1073 K) were calculated. Steels specimens were plane strain compressed and subjected to anodic potentiodynamic polarization scan in a different deaerated testing environment. The deformed specimens were characterized using electron backscattered diffraction system and Fourier transform infrared spectroscopy (FTIR)-imaging. The Cr₂O₃ peak from FTIR-imaging was captured, and area of the peak was calculated after anodic potentiodynamic polarization scan. The intensity of Cr₂O₃ peak was related to deformed microstructural features.

Keywords alloy chemistry, electron backscattered diffraction (EBSD), Fourier transform infrared spectroscopy (FTIR) imaging, passive film, stainless steels

1. Introduction

There have been enough scientific reports available about passive films developments, characterization and its mechanism on stainless steels (Ref 1). The researchers across the globe studied its stoichiometry, microstructure and electronic properties of the passive film (Ref 1-3). Hence, the surface passive films have been considered as a key technology for engineering applications particularly solar industry (Ref 4). The reports about oxide passive films have used various techniques. The surface chemical composition has been investigated by Auger electron spectroscopy (AES) and x-ray photoelectron spectroscopy (XPS). The Mott–Schottky measurement describes information about capacitance and potentials and has been used for studying semiconductor properties of the passive film. Mott–Schottky measurements reveal information about point defect density. Further, it also reveals information about the semiconductor type of passive film. The primary and secondary passive films were compared based on its film composition, thickness, structure and defect density for martensitic stainless steels (Ref 5). Both films contain iron and chromium oxides. The authors observed that pores were present in secondary passive films and higher defect density (Ref 5). Further, the authors have also observed the presence of pores in the secondary passive film.

It has been reported that a passive layer formed in a neutral 0.5 M NaCl solution have consisted of duplex structures (iron oxide and chromium oxide) (Ref 6). Generally, the passive film contributes protection of metallic materials from localized

corrosion such as pitting corrosion, stress corrosion cracking and intergranular corrosion (IGC). This has been long studied by researchers (electrochemists) due to interest arise from an academic and technological perspective. Thus, properties of passivity (barrier, adsorption and semiconductive) brought by both experimental and theoretical studies at nanometer and sub-nanometer scales have been studied (Ref 3). The effect of stresses (tensile and compressive) on surface passive film has also been discussed (Ref 7-9). It has been reported that tensile strained surface has the tendency to form a thicker surface passive layer than compressive strained (Ref 9). Further, it has been reported that crystallographic texture also affects anodic polarization behavior (Ref 8). There have been very few research reports about the usage of Raman and infrared spectroscopy in characterizing surface metal oxides (Ref 10-12) that relates to texture/microstructure other than authors previous work (Ref 13, 14). The orientation data thus collected during measurement are generally extracted from electron backscatter diffraction (EBSD) system, and it is often displayed by the crystal orientation maps called inverse pole figure (IPF).

At the nanoscale, the passivity behaviors usually exhibit heterogeneities in nature due to change in local chemical composition. The exact role of MnS inclusions on passivity breakdown is detailed with the help of electrochemical and microscopic techniques. Although with the advanced steel making technology, the presence of a very small amount of Sulfur cannot be avoided. It is present in steels in the form of manganese sulfide (MnS). The researchers have observed that the pitting initiation occurs at the site of MnS. By using in situ ex-environmental TEM technique, Zhang et al. (Ref 15) have discovered the dissolution sites of MnS.

Generally, chemical elements affect corrosion resistance by changing its nature/characteristics of the passive film (Ref 16-22). For stainless steels, the chemical elements such as chromium (Cr) improve corrosion resistance and nickel (Ni) stabilizes the austenite phase. Further, it is reported that copper (Cu) prevents anodic dissolution and promotes for passivation (Ref 23). The similar observation has been reported about the role of Cu for stainless steel grades (Ref 24). The chemical elements such as manganese (Mn) and molybdenum (Mo) (Ref 19) have been added to stainless steel material for resistance

N. Srinivasan and S. Senthil Kumaran, Department of Manufacturing Engineering, School of Mechanical Engineering, VIT Vellore Institute of Technology, Vellore, Tamil Nadu 632014, India. Contact e-mail: srinivasan.narayanan@vit.ac.in.

against pitting corrosion (Ref 16). In this study, stainless steels with different Ni and Cr contents were plastically deformed and their anodic polarization/passivation behavior was studied. The effect of deformation and alloy chemistry on the stability of passive films was studied by Fourier transform infrared spectroscopy (FTIR)-imaging and EBSD. Further, the effect of alloy chemistry on stacking fault energy (SFE) values and thermal conductivity was also discussed.

2. Experimental Methods

2.1 Materials and Methods

Three different grades of austenitic stainless steels were used in this study. The chemical composition of Sanicro 28™, AISI 316L and AISI 304L is shown in Table 1. The stainless steel strips were subjected to plane strain compression test to the true strains of 0.09, 0.26 and 0.58.

2.2 Electrochemical Test

All specimens were embedded in an epoxy resin and polished up to diamond finish (1 μm). Then the specimens were cleaned with soap solution, sonicated in acetone and dried, and electrical connection was provided using nichrome wire. The test solution used in this study was deaerated 0.5 M H₂SO₄, 1 M HCl, 1 M H₂SO₄ + 1.5 M HCl and 3 M HCl. The rationale for this is to induce passivity. Test solutions were prepared by using analytical grade reagents and distilled water. Prior to each anodic polarization test, the specimens were carefully lacquered exposing the surface area of 1 cm × 1 cm to the test solution. The deaeration was done using Argon gas for 45 min in a five-neck round-bottom flask at room temperature (26°C). The three electrode cell consists of working, reference and auxiliary electrodes. The working electrode was stainless steel specimens, the reference electrode was saturated calomel electrode (SCE), and an auxiliary electrode was platinum used for this study. The open-circuit potential was established, and then, all specimens were monitored for 5 min at OCP for stabilization. Then, anodic potentiodynamic polarization was carried out. The applied potential was – 300 mV with respect to SCE, and the current was recorded. Further, the potential was allowed upward till transpassive region 1100 mV with respect to SCE. The experimental conditions for all specimens remained the same, such as scan rate, exposed area and OCP. All specimens after anodic polarization were cleaned and dried.

2.3 EBSD Measurements

Electropolishing was carried out for EBSD measurements. All specimens were electropolished using Struers™ Lectropol-5 machine. The electropolishing test solution (electrolyte) con-

sists of methanol and perchloric acid. The electropolishing parameters such as voltage and temperature were set at 15 V and – 20°C, respectively. The EBSD systems consist of TSL–OIM EBSD™ that was used as a post-processing software. The image quality (IQ) and IPF maps were extracted.

2.4 FTIR-Imaging Measurements

The surface passive film, particularly the Cr₂O₃, was quantified using FTIR-imaging. This was carried out in Bruker™ 300-Hyperion machine. The area under the peak of Cr₂O₃ was calculated by using a commercial software Opus 6.5™. The higher value of the area under the peak indicated that the stronger presence of Cr₂O₃. Similarly, the faint intensity of FTIR-imaging at wavenumber of 660 cm⁻¹ indicated the weaker presence of Cr₂O₃.

2.5 Thermal Conductivity Measurement

Thermophysical material properties such as thermal conductivity and diffusivity were calculated using a laser flash method. This was carried out in LINSEIS™ LFA 1000 machine. Further details can be found elsewhere (Ref 14).

3. Results and Discussion

The electrochemical technique generally offers a quick and simple way to assess electrochemical properties, corrosion mechanism and corrosion rate. It is based on the charge-transfer mechanism to determine the corrosion rate of metal by changing the potential of the working electrode and monitoring/recording current simultaneously. The potentiodynamic, potentiostaircase and cyclic voltammetry are the different types of polarization testing methods. Anodic polarization scan changes the potential in a more positive direction (noble) (Fig. 1) by making the working electrode to lose electrons, whereas in cathodic polarization, electrons are added to the working electrode. Anodic polarization curve consists of active, passive and transpassive regions for materials that exhibit passivity (Fig. 1). In passive regions (as marked in Fig. 1), the current value/current density is usually lower than the active region. The definition and change in anodic polarization parameters such as E_{crit} , i_p , E_{corr} and its behavior with deformed microstructure are detailed elsewhere (Ref 13).

The increase in current density in anodic polarization curves indicated that difficulty in achieving passivity after deformation. The plastic deformation of austenitic stainless steels gives rise to martensite formation and generation of dislocation substructure. The martensite induced by cold working of metastable stainless steels directly affects corrosion properties in acidic test solutions. The anodic polarization curve is very sensitive to alloy composition, and the behavior is usually

Table 1 Alloy composition used in this study (wt.%)

	C	P	Mn	S	Cr	Mo	Si	Ni	Cu	N
Sanicro 28™	0.020	0.025	2.0	0.015	27.00	3.6	0.60	31.0	1.09	...
AISI 316L	0.020	0.010	1.0	0.020	16.25	2.3	0.38	10.73	...	0.10
AISI 304L	0.029	0.025	1.78	0.010	18.01	...	0.20	8.21	...	0.037

dependent on the exposed testing environment. Hence, it is decided to examine various grades of stainless steels in a different test solution. These are deaerated of test solution of

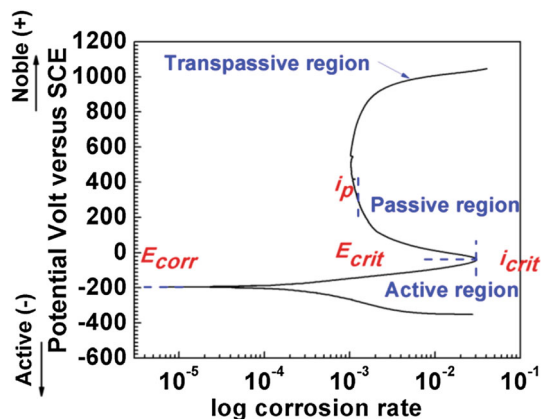


Fig. 1 Polarization curve showing anodic regime consisting of three regions. The anodic polarization parameters are marked

0.5 M H₂SO₄, 1 M HCl, 1 M H₂SO₄ + 1.5 M HCl and 3 M HCl. The as-received Sanicro 28™ specimens were exposed to 0.5 M H₂SO₄, 1 M HCl, 1 M H₂SO₄ + 1.5 M HCl and 3 M HCl test solution, and anodic polarization curve was recorded (Fig. 2a). The better passivity behavior was observed in Sanicro 28™ specimens in the as-received state in all test solutions except in 3 M HCl (Fig. 2a). In 3 M HCl, the two anodic peaks were observed (Fig. 2a and b). During anodic potentiodynamic polarization scan, the first peak is to correspond to iron dissolution. Dissolution of different phases leads to a second anodic peak for austenitic stainless steels in acidic media as revealed by different researchers (Ref 25-27). The objective of this study is to induce passivity; hence, in this paper, the experiment is designed to discard further analysis/reading of this result. The passivity was induced for AISI 304L, AISI 316L and Sanicro 28™ in as-received and deformed specimens in 0.5 M H₂SO₄. The measured potential values with respect to the reference electrode (saturated calomel electrode) at different regions of the anodic polarization curve indicated that at 3 M HCl, metastable pits were evident (Fig. 2b). The same was observed after imposing deformation in Sanicro 28™ specimens (Fig. 2c).

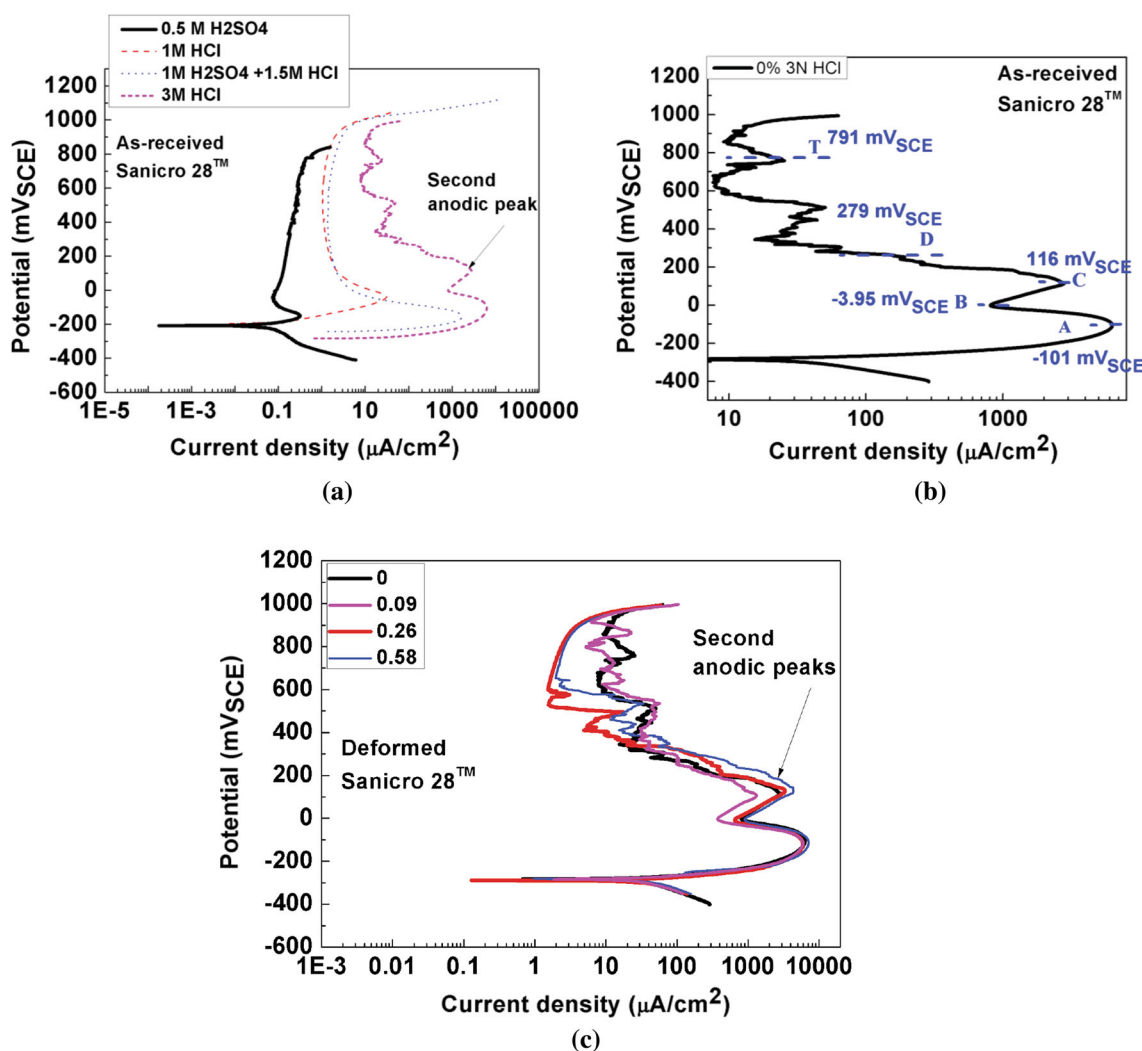


Fig. 2 Anodic potentiodynamic curves of Sanicro 28™ specimens (a) as-received state tested at the different deaerated solutions (0.5 M H₂SO₄, 1 M HCl, 1 M H₂SO₄ + 1.5 M HCl, 3 M HCl), and (c) deformed specimens tested at 3 N HCl. The presence of a second anodic peak is noticed at 3 N HCl in (a) as-received and (b) deformed specimens

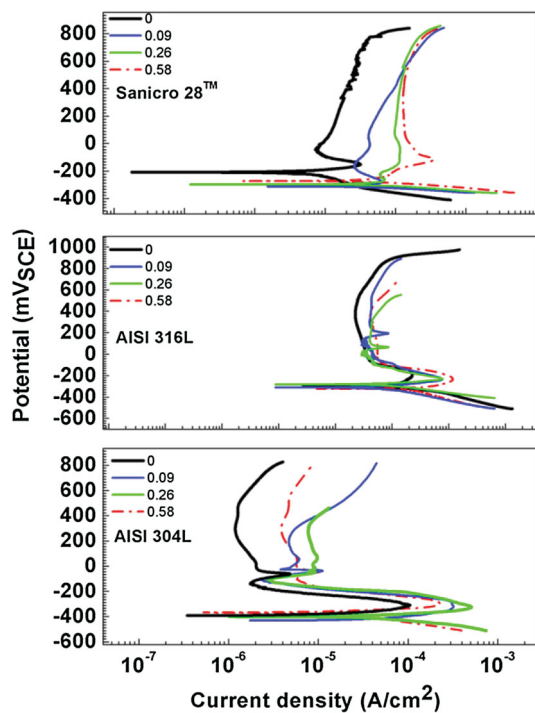


Fig. 3 Anodic potentiodynamic polarization curves of Sanicro 28™, AISI 316L and AISI 304L stainless steels tested at 0.5 M H₂SO₄

Though clear passivity was observed in all specimens of steels grades (Fig. 3), there exists a difference in anodic potentiodynamic curves with deformation between Sanicro 28™ and other grades (Fig. 3). Hence, it was decided to characterize the microstructure of as-received and deformed specimens of Sanicro 28™ (Fig. 4). The average grain size of as-received specimens of Sanicro 28™ as estimated from EBSD system was 160 μm (Fig. 4a). The interrupted post-deformation microstructure of Sanicro 28™ specimens was developed by EBSD system (Fig. 4a-d) as revealed through IQ and IPF maps. The signatures of deformed microstructures such as the development of orientation gradients (Fig. 4b and c), generation of slip bands (Fig. 4b) and strain localizations (Fig. 4c) were noticed. The orientation gradients, slip lines/slip bands and strain localizations were developed as a result of progressive deformation for all grades. Due to brevity, only Sanicro 28™ deformed microstructures were included in this study.

The material parameter such as stacking fault energy (SFE) and thermal conductivity usually depend on alloy chemistry. In this study, the SFE value was estimated and the thermal conductivity value was calculated for all specimens. The material with higher SFE has less separation between partial dislocations and material that has lower SFE create Shockley partial dislocations and forms planar dislocation substructure. The plastically deformed microstructure, particularly lower SFE materials (austenitic stainless steels and copper) is interesting and offers unique microstructural features. Further, SFE decides deformation and transformation mechanism of metallic materials and the mechanical behavior of materials. Generally, austenitic stainless steels exhibit face-centered cubic (fcc) crystal structure. When these steels undergo the displacive transformation, martensite does form. There is ϵ martensite having hexagonal crystal structure (hcp) and α' martensite that

exhibits body-centered cubic structure. Formation of ϵ martensite (hcp) and α' martensite (bcc) is usually evident at low and high deformation level, respectively. At the higher degree of deformation, α' martensite forms at the expense of ϵ martensite. Deformed microstructures of metastable stainless steels have shear bands, micro-bands and dislocations pile-up. The α' martensite nucleates at intersections of shear bands. α' martensite increases the work-hardening of steels. This transformation of α' martensite again depends on alloy chemistry, temperature and strain rate.

The SFE of Sanicro 28™ was estimated to be 57 mJ/m^2 . This is the highest compared to AISI 316L and AISI 304L steels. The thermal conductivity value at 298 K was 10 W/mK. This is for Sanicro 28™ materials. While this is the lowest among the other materials (AISI 316L and AISI 304L) tested at the same temperature (Fig. 5). The monotonic increase in thermal conductivity value was noticed. The overall trend that emerged was that the thermal conductivity value was depended on temperature (Fig. 5).

The local corrosion probing techniques such as atomic force microscopy (AFM), scanning electrochemical microscopy (SECM), scanning tunneling microscopy (STM), transmission electron microscopy (TEM), time-of-flight secondary ions mass spectroscopy (ToF-SIMS) (Ref 28) and energy-dispersive x-ray spectroscopy (EDX) (Ref 38) have been used extensively to understand and to characterize the passive film and local corrosion mechanism. These techniques revealed that Cl^- ions play a role in passivity breakdown. In general, STM and AFM have been extensively used by the researchers to study oxide passive films. The STM and AFM results have revealed that the presence of Cr in the passive film is discontinuous and random (Ref 3). Passivity breakdown happens at discrete random locations, and this leads to the formation of stable/metastable pits. These pits act as nucleation sites for many localized corrosion phenomena such as stress corrosion cracking and pitting corrosion.

The measurement of electrochemical and electrical properties at the nano/micro scale is critical to tailor microstructure and corrosion properties. Hence, the electrochemical and electronic properties have been investigated by the researchers for stainless steels and other alloys. AFM is a tool for microscopic investigation of surface properties, and researchers have started to use since the 80's. With the advent of scanning probing microscopes, electrical conductivity, capacity, charges and surface potential can be measured, (Ref 29). Current sensing AFM (CS-AFM) also called conducting AFM (C-AFM) studied the passive layer formed over different phases of duplex stainless steels and simultaneously measured the surface topography and current distribution. (Ref 30, 31). Guo et al. (2018) have demonstrated that using this technique, electrical properties of passive film were studied at 300 and 400 $^\circ\text{C}$ for duplex stainless steels. Based on their detailed study, current contribution from austenite phase was higher and the passive film formed over austenitic phases exhibited good electrical conductivity (Ref 32). The local impedance spectroscopy in AFM mode has revealed the extent of IGC attack. This method was able to provide insight into the early occurrence of IGC compared to standard DL-EPR test (Ref 33). Electrochemical scanning tunneling microscopy (ECSTM) has also been used to observe passive behavior at grain boundaries of Cu (Ref 34). With this ECSTM technique, the same authors have observed that the thicker passive film was formed at random grain boundaries in another study (Ref 35). In contrast, Lombordia

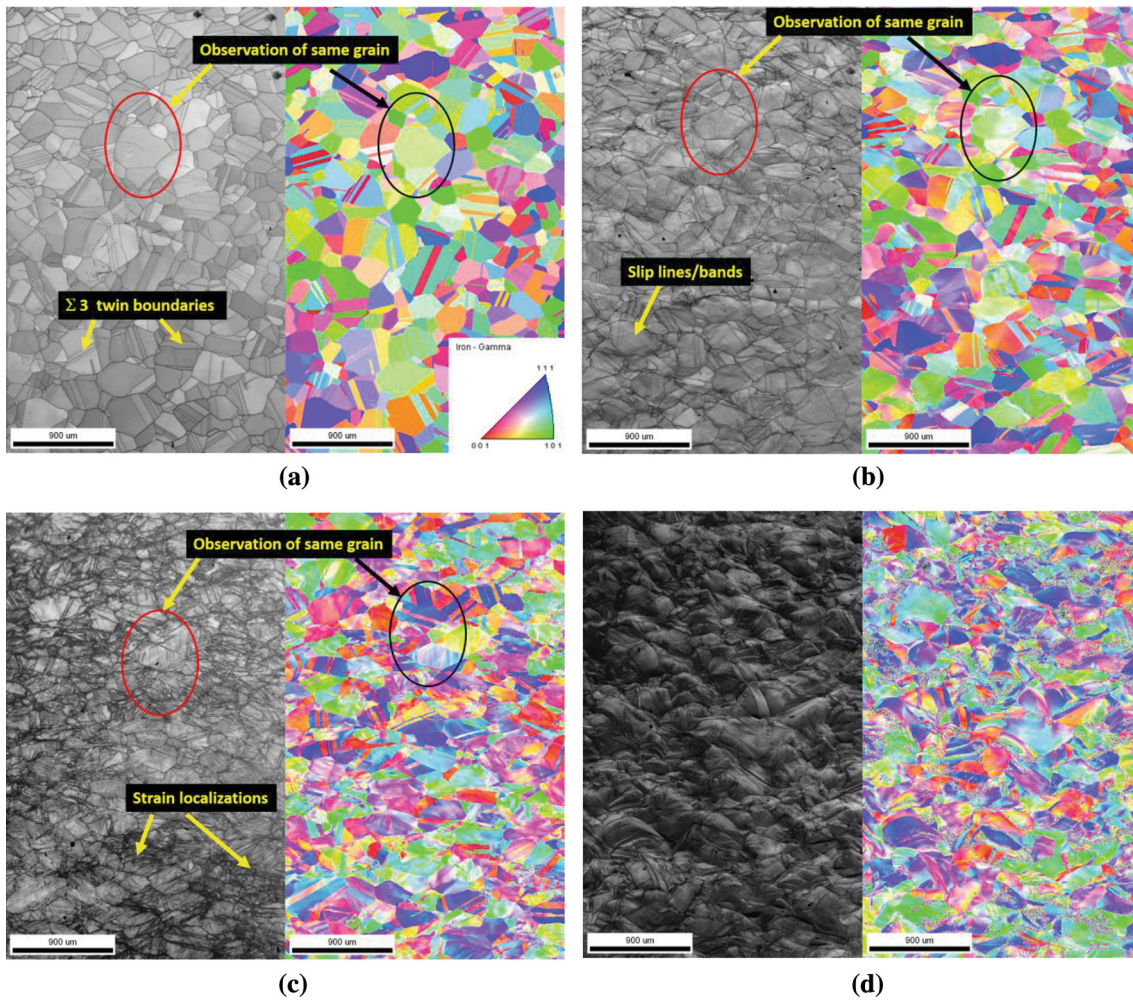


Fig. 4 Images IQ (gray scale) and IPF (color) are from EBSD system of Sanicro 28TM specimens. (a) as-received state and the identical areas are observed after imposing a true strain of (b) 0.09, (c) 0.26 and (d) 0.58. In (a), inset shows grain orientations having IPF color legend crystal directions of [100], [110] and [111] in red, green and blue, respectively (Color figure online)

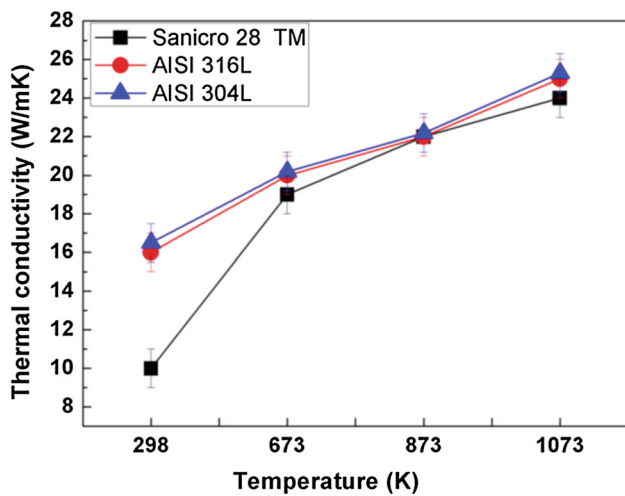


Fig. 5 Evaluation of thermal conductivity at different temperatures of Sanicro 28TM, AISI 316L and AISI 304L stainless steels

et al. (Ref 36) have observed that coherent twin boundaries exhibited resistance to IGC as observed by in situ STM. It is reported from the tools of nanoscale such as STM and AFM

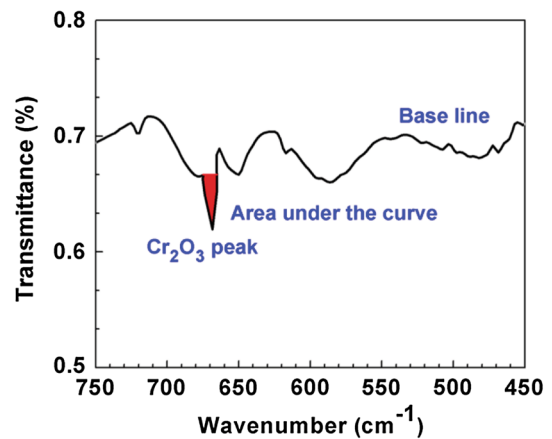


Fig. 6 Transmittance (%) vs. wave number for Cr₂O₃

oxide passive films of stainless steels contain a discontinuous distribution of Cr in oxide passive films (Ref 3, 41). Scanning tunneling spectroscopy (STS) is a special mode in STM to examine local surface electronic density of states (Ref 37). Thus, both AFM and STM and its multi-purpose variants

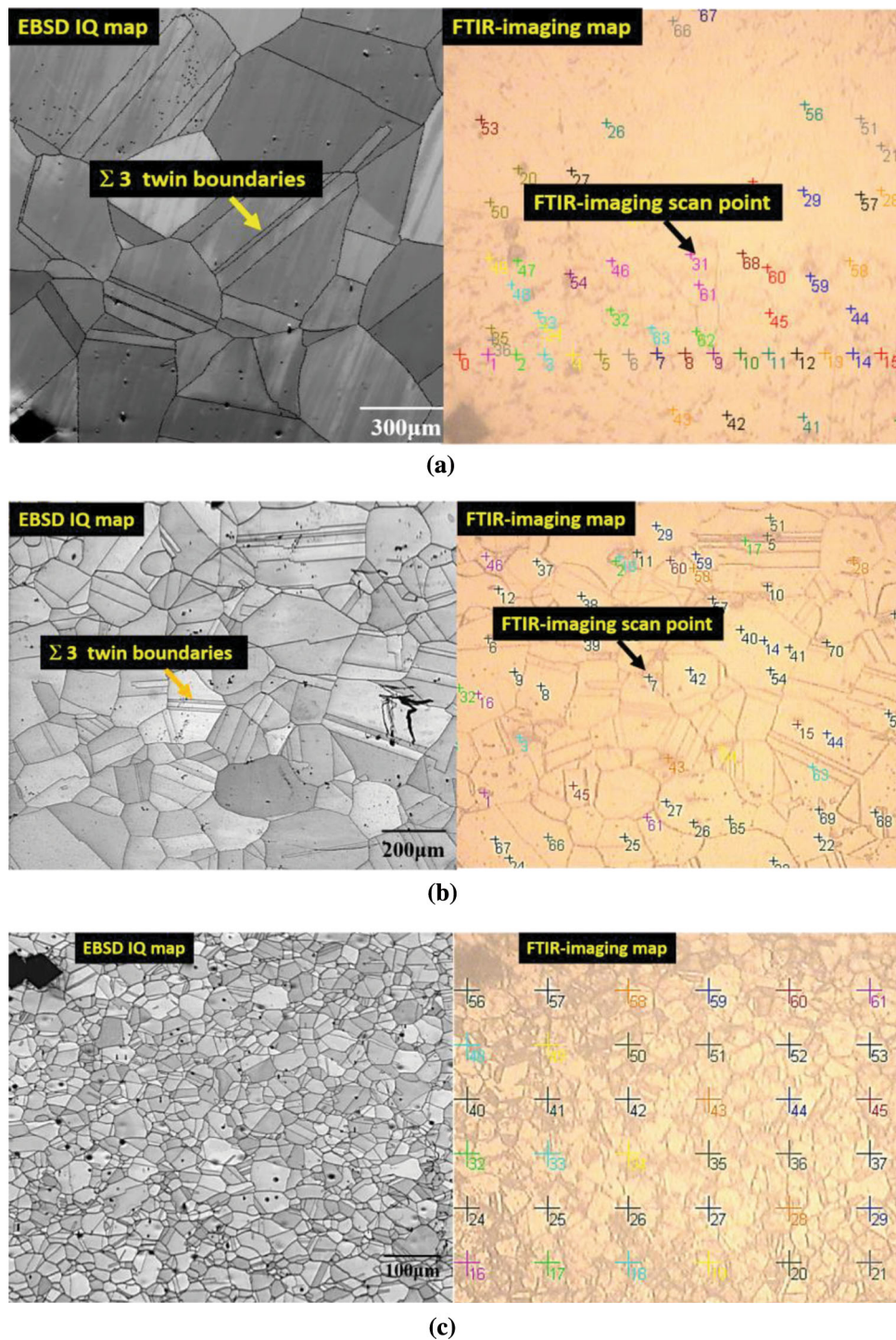


Fig. 7 Observation of same the area of microstructural features assessed from EBSD and FTIR-imaging scanning point for possible correlation of (a) Sanicro 28™, (b) AISI 316L and (c) AISI 304L in as-received state

(mode) have been playing an important role in understanding the localized phenomenon.

In addition, with the advent of microscopy and spectroscopic techniques, further, the local corrosion probing tools can be combined to unravel the mechanism of passivity at nano/micro scale, to refine the understanding. The combined techniques of EBSD and AFM have provided complete dataset of plastic deformation of phases of duplex stainless steels (Ref 38). Further, EBSD and ECSTM have been used for direct

observation of grain boundary and its susceptibility to IGC (Ref 36) and passivation behavior of copper (Ref 39). The passivation behavior of copper has been widely explored by researchers. Chen et al. (Ref 34) have used ECSTM to observe passivation behavior at grain boundaries of microcrystalline copper. They observed that, the thicker passivation behavior was observed at random grain boundaries than coherent twin boundaries. This is in line with the Chen et al. (Ref 34). In another study, the Cu surface morphology has been observed

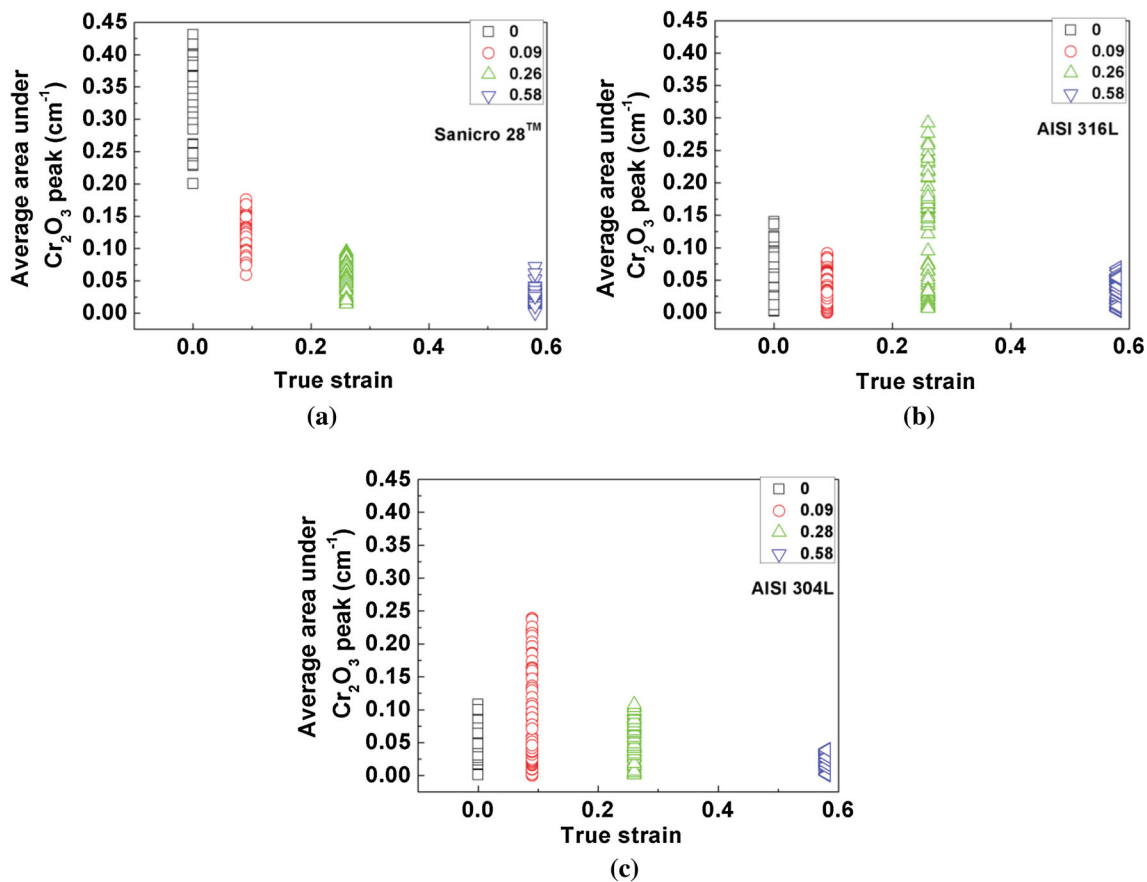


Fig. 8 Average area under Cr₂O₃ peaks vs. true strain of as-received and deformed specimens of (a) Sanicro 28™, (b) AISI 316L and (c) AISI 304L

after polarization experiment. This result has been done by the direct combination of STM and FTIR, and the absorption and corrosion inhibition at 0.1 M HCl have been investigated (Ref 40).

In another study, accurate atomic sites of dissolution by different techniques have been applied using in situ environmental TEM to extract atomic information about dissolution for stainless steels and Al-2024 alloys (Ref 15). Despite the extensive research in this field, using the techniques mentioned above, the role of local metallurgical effect on passivity breakdown and initiation of pitting for stainless steel has been insufficiently investigated, except few studies (Ref 39) other than authors' previous investigations (Ref 13). Further, all these techniques as discussed previously have been extensive and laborious. Hence, it has been decided to use a relatively simple technique in this study. Therefore, the combination of EBSD and FTIR-imaging has been used in this research work. With this EBSD + FTIR-imaging, the possibility of having larger multiple scans to produce statistically significant data is apparent.

Hence, it was decided to study passive film on the substrate microstructure post-potentiodynamic tests through FTIR-imaging and correlate with EBSD measurements. The associated developments of grains were observed directly. The EBSD reveals information about crystal orientation and nature of grain boundary while FTIR-imaging deals about oxide characterization. The wavenumber around 660 cm⁻¹ corresponds to Cr₂O₃

metal oxide as plotted in transmittance mode (Fig. 6). The combined techniques of EBSD and FTIR-imaging have enabled to observe and examine the same grains (Fig. 7). The need was felt for direct observation of grains. Hence, the experiment was designed to extract information (Cr₂O₃ peak) from FTIR-imaging to relate to microstructural features. The FTIR-imaging scanning point has the capability to probe at the different microstructural locations and extract information. Thus, Cr₂O₃ peak was measured and area under each peak over its quantified and related to microstructural features. The higher intensity and continuous presence of Cr₂O₃ are the key that determines the stability of passive films. This, in turn, depends on microstructural and/or sub-structural features. The FTIR-imaging probed the post-corrosion microstructures and quantified the intensity of Cr₂O₃. The average area (collection of data points of 100 such peaks) for as-received Sanicro 28™ was 0.34 cm⁻¹ and for 0.09 true strain 0.12 cm⁻¹ (Fig. 8a). The gradual decrease in the average value after imposing plastic strain was not noticed for other grades of specimens (Fig. 8b and c) though the atomic packing density of BCC crystallite is less than the FCC structure. At this juncture, it is important to appreciate the deformed microstructure of AISI 316L and AISI 304L. These materials contain α' martensite and dislocation pile-ups. The presence of α' martensite particles and associated tensile stress after large plastic deformations minimized the corrosion deterioration as reported in this Ref 8.

In this work also, the same was observed (Fig. 8b and c). The microstructure of AISI 316L and AISI 304L contains many deformed features as compared to Sanicro 28™. The Sanicro 28™ material does not have the tendency to form α' martensite. It contains austenitic FCC structure after deformation. The general understanding of the role of α' martensite is that reduced corrosion resistance in acidic solutions (Ref 41, 42). Further, it has been reported that amount of α' martensite has the least importance (Ref 21) and the cold working of stainless steels affect (Ref 21), does not affect (Ref 43) the corrosion resistance. Further, it has been reported that corrosion resistance depends on other microstructural features along with the presence of α' martensite. The indirect role of α' martensite has been discussed. This inconsistency has been reported about the exact role of α' martensite and many researchers have expressed different interpretations (Ref 8, 41, 44-46).

However, the possibility of the direct role of dislocation on corrosion deterioration and the indirect role of α' martensite cannot be ruled out. The further investigation on possible reason after carefully isolating the microstructural features such as types of dislocation arrangements, martensite particles and deformation bands is needed. Hence at this stage, it is admitting that a fairly complex mechanism is at play. The sophisticated small (micro/nano) scale analysis along with the conventional electrochemistry measurement is needed. Thus, the use of the right combination of techniques of in situ spectroscopic and microscopic studies can provide comprehensive information about the mechanism at the nanoscale.

4. Conclusions

The following can be concluded from the study:

- The grades of stainless steels with the difference in chemical composition were deformed (the true strain of 0.09, 0.26 and 0.58), and anodic potentiodynamic experiments were carried out for all specimens. The presence of metastable pit was evident in deaerated 3 M HCl test solution both in as-received state and deformed specimens of Sanicro 28™ grades. The clear passivity was established in 0.5 M H₂SO₄, 1 M HCl, 1 M H₂SO₄ + 1.5 M HCl test solutions for Sanicro 28™ grades. The passivity was induced in the deaerated test solution of 0.5 M H₂SO₄ in as-received and deformed specimens of AISI 304L, AISI 316L and Sanicro 28™.
- These grades differ in alloy chemistry; hence, SFE was estimated and thermal conductivities at different temperatures (298, 673, 873 and 1073 K) were calculated.
- Direct observation of grain had enabled to observe the development of orientation gradients, slip lines/slip bands and strain localizations after progressive deformation for Sanicro 28™ grades.
- The average area under the Cr₂O₃ peak was quantified for as-received and deformed specimens of all stainless steel grades. Further, the EBSD and FTIR-imaging enabled for direct inspection of Cr₂O₃ peak and its peak was quantified and related to microstructural features.
- The average area of Cr₂O₃ peak for Sanicro 28™ specimen was decreased monotonically from as-received to all deformed specimens, and the change was significant. Such a significant monotonic decrease was not

observed for AISI 316L and AISI 304L specimens. The trend was not clearly emerged along with progressive deformation.

References

1. V. Maurice and P. Marcus, Progress in Corrosion Science at Atomic and Nanometric Scales, *Prog. Mater. Sci.*, 2018, **95**, p 132–171
2. N.E. Hakiki, Comparative Study of Structural and Semiconducting Properties of Passive Films and Thermally Grown Oxides on AISI, 304 Stainless Steel, *Corros. Sci.*, 2011, **53**, p 2688–2699
3. V. Maurice and P. Marcus, Current Developments of Nanoscale Insight into Corrosion Protection by Passive Oxide Films, *Curr. Opin. Solid State Mater. Sci.*, 2018, **22**, p 156–167
4. S.W. Glunz and F. Feldmann, SiO₂ Surface Passivation Layers—A Key Technology for Silicon Solar Cells, *Sol. Energy Mater. Sol. Cells*, 2018, **185**, p 260–269
5. C. Man, C. Dong, Z. Cui, K. Xiao, Q. Yu, and X. Li, A Comparative Study of Primary and Secondary Passive Films Formed on AM355 Stainless Steel in 0.1 M NaOH, *Appl. Surf. Sci.*, 2018, **427**, p 763–773
6. R. Babic, Semiconducting Properties of Passive Films on AISI, 304 and 316 Stainless Steels, *J. Electroanal. Chem.*, 1993, **358**, p 143–160
7. F. Navai, Effects of Tensile and Compressive Stresses on the Passive Layers Formed on a Type 302 Stainless Steel in a Normal Sulphuric Acid Bath, *J. Mater. Sci.*, 1995, **30**, p 1166–1172
8. B. Ravi Kumar, R. Singh, B. Mahato, P.K. De, N.R. Bandyopadhyay, and D.K. Bhattacharya, Effect of Texture on Corrosion Behavior of AISI, 304L Stainless Steel, *Mater. Charact.*, 2005, **54**, p 141–147
9. F. Navai and O. Debbouz, AES Study of Passive Films Formed on a Type 316 Austenitic Stainless-Steels in a Stress Field, *J. Mater. Sci.*, 1999, **34**, p 1073–1079
10. D.K. Ottesen and A.S. Nagelberg, Infrared Spectroscopic Studies of Surface Oxides, *Thin Solid Films*, 1980, **73**, p 347–352
11. I.E. Wachs, Raman and IR Studies of Surface Metal Oxide Species on Oxide Supports: Supported Metal Oxide Catalysts, *Catal. Today*, 1996, **27**, p 437–455
12. S. Ramya, T. Anita, H. Shaikh, and R.K. Dayal, Laser Raman Microscopic Studies of Passive Films Formed on Type 316LN Stainless Steels During Pitting in Chloride Solution, *Corros. Sci.*, 2010, **52**, p 2114–2121
13. N. Srinivasan, V. Kain, N. Birbilis, B.S. Kumar, M.N. Gandhi, P.V. Sivaprasad, G. Chai, A. Lodh, P.M. Ahmedabadi, and I. Samajdar, Plastic Deformation and Corrosion in Austenitic Stainless Steel: A Novel Approach Through Microtexture and Infrared Spectroscopy, *Corros. Sci.*, 2016, **111**, p 404–413
14. N. Srinivasan, B. Sunil Kumar, V. Kain, N. Birbilis, S.S. Joshi, P.V. Sivaprasad, G. Chai, A. Durgaprasad, S. Bhattacharya, and I. Samajdar, Defining the Post-Machined Sub-surface in Austenitic Stainless Steels, *Metall. Mater. Trans. A*, 2018, **49**, p 2281–2292
15. B. Zhang and X. Ma, A Review—Pitting Corrosion Initiation Investigated by TEM, *J. Mater. Sci. Technol.*, 2019, **35**, p 1455–1465
16. A. Pardo, M.C. Merino, A.E. Coy, F. Viejo, R. Arrabal, and E. Matykina, Pitting Corrosion Behaviour of Austenitic Stainless Steels—Combining Effects of Mn and Mo Additions, *Corros. Sci.*, 2008, **50**, p 1796–1806
17. E.E. Oguzie, J. Li, Y. Liu, D. Chen, Y. Li, K. Yang, and F. Wang, The Effect of Cu Addition on the Electrochemical Corrosion and Passivation Behavior of Stainless Steels, *Electrochim. Acta*, 2010, **55**, p 5028–5035
18. Z. Wang, L. Zhang, Z. Zhang, and M. Lu, Combined Effect of pH and H₂S on the Structure of Passive Film Formed on Type 316L Stainless Steel, *Appl. Surf. Sci.*, 2018, **458**, p 686–699
19. L.V. Taveira, M.F. Montemor, M. Da Cunha Belo, M.G. Ferreira, and L.F.P. Dick, Influence of Incorporated Mo and Nb on the Mott-Schottky Behaviour of Anodic Films Formed on AISI, 304L, *Corros. Sci.*, 2010, **52**, p 2813–2818
20. A. Sadough Vanini, J.P. Audouard, and P. Marcus, The Role of Nitrogen in the Passivity of Austenitic Stainless Steels, *Corros. Sci.*, 1994, **36**, p 1825–1834

21. A. Barbucci, G. Cerisola, and P.L. Cabot, Effect of Cold-Working in the Passive Behavior of 304 Stainless Steel in Sulfate Media, *J. Electrochem. Soc.*, 2002, **149**, p B534–B542
22. M.Z. Yang, Q. Yang, and J.L. Luo, Effects of Hydrogen on Passive Film and Corrosion of AISI 310 Stainless Steel, *Corros. Sci.*, 1999, **41**, p 741–745
23. X. Zhang, J. Zhao, T. Xi, M.B. Shahzad, C. Yang, and K. Yang, Dissolution and Repair of Passive Film on Cu-Bearing 304L Stainless Steels Immersed in H₂SO₄ Solution, *J. Mater. Sci. Technol.*, 2018, **34**, p 2149–2159
24. A. Pardo, M.C. Merino, M. Carboneras, F. Viejo, R. Arrabal, and J. Munoz, Influence of Cu and Sn Content in the Corrosion of AISI 304 and 316 Stainless Steels in H₂SO₄, *Corros. Sci.*, 2006, **48**, p 1075–1092
25. M. Rockel, Interpretation of Second Anodic Current Maximum of Polarization Curves of Sensitized Chromium Steels in 1 N H₂SO₄, *Corrosion*, 1971, **21**, p 95–103
26. L. Felloni, S.S. Traverso, G.L. Zucchini, and G.P. Cammarota, Investigation on the Second Anodic Current Maximum on the Polarization Curves of Commercial Stainless Steels in Sulphuric Acid, *Corros. Sci.*, 1973, **13**, p 773–789
27. N. Srinivasan, A.K. Revelly, V. Kain, I. Samajdar, C.R. Hutchinson, and P. Sivaprasad, Anodic Polarization Behavior of Cold Worked Austenitic Stainless Steel, *Adv. Mater. Res.*, 2013, **794**, p 632–642
28. S. Al Saadi, Y. Yi, P. Cho, C. Jang, and P. Beeley, Passivity Breakdown of 316L Stainless Steel During Potentiodynamic Polarization in NaCl Solution, *Corros. Sci.*, 2016, **111**, p 720–727
29. J. Yin, C. D'Haese, and B. Nyssen, Surface Electrical Properties of Stainless Steel Fibres: An AFM-Based Study, *Appl. Surf. Sci.*, 2015, **330**, p 65–73. <https://doi.org/10.1016/j.apsusc.2014.12.188>
30. T. Souier, F. Martin, C. Bataillon, and J. Cousty, Local Electrical Characteristics of Passive Films Formed on Stainless Steel Surfaces by Current Sensing Atomic Force Microscopy, *Appl. Surf. Sci.*, 2010, **256**, p 2434–2439
31. T. Souier and M. Chiesa, Effect of Surface Conditions and Strain Hardening on the Passivity Breakdown of 304 Stainless Steel, *J. Mater. Res.*, 2012, **27**, p 1580–1588
32. L.Q. Guo, B.J. Yang, J.Y. He, and L.J. Qiao, Local Electrical Properties of Thermally Grown Oxide Films Formed on Duplex Stainless Steel Surfaces, *Appl. Surf. Sci.*, 2018, **444**, p 48–55. <https://doi.org/10.1016/j.apsusc.2018.03.047>
33. A. Arutunow, K. Darowicki, and A. Zieliński, Atomic Force Microscopy Based Approach to Local Impedance Measurements of Grain Interiors and Grain Boundaries of Sensitized AISI, 304 Stainless Steel, *Electrochim. Acta*, 2011, **56**, p 2372–2377
34. H. Chen, V. Maurice, L.H. Klein, L. Lapeire, K. Verbeken, H. Terryn, and P. Marcus, Grain Boundary Passivation Studied by In Situ Scanning Tunneling Microscopy on Microcrystalline Copper, *J. Solid State Electrochem.*, 2015, **19**, p 3501–3509
35. H. Chen, M. Bettayeb, V. Maurice, L.H. Klein, L. Lapeire, K. Verbeken, H. Terryn, and P. Marcus, Local Passivation of Metals at Grain Boundaries: In Situ Scanning Tunneling Microscopy Study on Copper, *Corros. Sci.*, 2016, **111**, p 659–666
36. E. Martinez-Lombardia, L. Lapeire, V. Maurice, I. De Graeve, K. Verbeken, L.H. Klein, L.A.I. Kestens, P. Marcus, and H. Terryn, In Situ Scanning Tunneling Microscopy Study of the Intergranular Corrosion of Copper, *Electrochem. Commun.*, 2014, **41**, p 1–4
37. V. Maurice and P. Marcus, Passive Films at the Nanoscale, *Electrochim. Acta*, 2012, **84**, p 129–138
38. S. Fréchar, F. Martin, C. Clément, and J. Cousty, AFM and EBSD Combined Studies of Plastic Deformation in a Duplex Stainless Steel, *Mater. Sci. Eng. A*, 2006, **418**, p 312–319
39. M. Bettayeb, V. Maurice, L.H. Klein, L. Lapeire, K. Verbeken, and P. Marcus, Combined In Situ Microstructural Study of the Relationships Between Local Grain Boundary Structure and Passivation on Microcrystalline Copper, *Electrochim. Acta*, 2019, **305**, p 240–246
40. M.R. Vogt, R.J. Nichols, O.M. Magnussen, and R.J. Behm, Benzotriazole Adsorption and Inhibition of Cu(100) Corrosion in HCl: A Combined In Situ STM and In Situ FTIR Spectroscopy Study, *J. Phys. Chem. B.*, 1998, **102**, p 5859–5865
41. K. Elayaperumal, P.K. De, and J. Balachandra, Passivity of Type 304 Stainless Steel—Effect of Plastic Deformation, *Corrosion.*, 1972, **28**, p 269–273
42. A.S. Hamada, L.P. Karjalainen, and M.C. Somani, Electrochemical Corrosion Behaviour of a Novel Submicron-Grained Austenitic Stainless Steel in an Acidic NaCl Solution, *Mat. Sci. Eng. A.*, 2006, **431**, p 211–217
43. S.V. Phadnis, A.K. Satpati, K.P. Muthe, J.C. Vyas, and R.I. Sundaresan, Comparison of Rolled and Heat Treated SS304 in Chloride Solution Using Electrochemical and XPS Techniques, *Corros. Sci.*, 2003, **45**, p 2467–2483
44. X.F. Fang and W. Dahl, Strain Hardening and Transformation Mechanism of Deformation Induced Martensite Transformation in Metastable Austenitic Stainless Steels, *Mat. Sci. Eng. A.*, 1991, **141**, p 189–198
45. L. Peguet, B. Malki, and B. Baroux, Influence of Cold Working on the Pitting Corrosion Resistance of Stainless Steels, *Corros. Sci.*, 2007, **49**, p 1933–1948
46. L. Peguet, B. Malki, and B. Baroux, Effect of Austenite Stability on the Pitting Corrosion Resistance of Cold Worked Stainless Steels, *Corros. Sci.*, 2009, **51**, p 493–498

Publisher's Note Springer Nature remains neutral with regard to jurisdictional claims in published maps and institutional affiliations.